Version of Record: https://www.sciencedirect.com/science/article/pii/S0144861719309737
Manuscript_6d765a64cee2f950f2df10dac86ad459

# Anisotropic Nanocellulose Gel–Membranes for Drug Delivery: Tailoring Structure and Interface by Sequential Periodate–Chlorite Oxidation

Sven F. Plappert[†‡], Falk W. Liebner[†], Johannes Konnerth[§], Jean-Marie Nedelec[‡*]

[†]Division of Chemistry of Renewable Resources, University of Natural Resources and Life Sciences Vienna, Konrad-Lorenz-Straße 24, 3430 Tulln, Austria

[‡] Université Clermont Auvergne, CNRS, SIGMA Clermont, ICCF, F-63000 Clermont-Ferrand, France

[§] Institute of Wood Technology and Renewable Materials, University of Natural Resources and Life Sciences Vienna, Konrad-Lorenz-Straße 24, A-3430 Tulln, Austria

* corresponding author: jean-marie.nedelec@sigma-clermont.fr

**KEYWORDS**

2,3-dicarboxyl cellulose, cellulose nanofibers, anisotropic gel membranes, transdermal drug delivery patches, non-steroidal anti-inflammatory drugs, piroxicam

**ABSTRACT**

This study investigates periodate–chlorite oxidation as a pretreatment to tailor the surface charge density of cellulose nanofibers employed in open-porous anisotropic hydrogel membranes for transdermal drug delivery. The obtained materials feature high specific surface (≤ 500 $m^2 g^{-1}$, BET), small average pore size (ca. 40 nm) and tunable surface charge, which are key properties for adsorption and slow release of charged drug molecules. Loading of the non-steroidal anti-inflammatory drug (NSAID) piroxicam (PRX) into the membranes confirmed that the extent of loading is governed by surface charge density and carboxylate group content, respectively, which can be controlled by the oxidation procedure within the range of 0.74 to 2.00 mmol $g^{-1}$. Prolonged release of PRX over several hours was observed upon exposure of the loaded membranes to simulated human skin fluid demonstrating the applicability as drug delivery patches.

## 1 INTRODUCTION

Assembly of colloidal particles such as nanocellulose into porous bulk structures can afford materials of high specific interface which can be utilized for applications relying on interfacial chemical and physical processes, such as chemi- and physisorption. In case the interstitial liquid phase filling the interconnected pore system of the colloidal solid is water, respective

materials are classified as hydrogels. The latter have demonstrated great potential for biomedical applications including wound dressings (Hakkarainen et al., 2016; Leppiniemi et al., 2017), cartilage implants (Ahrem et al., 2014), scaffolds for tissue engineering (Bonilla, Lopez-Sanchez, Gidley, & Stokes, 2016; Deng et al., 2010; Liu et al., 2017; Van Vlierberghe, Dubruel, & Schacht, 2011; Zaborowska et al., 2010) and drug delivery (Abeer, Mohd Amin, & Martin, 2014; Hujaya, Lorite, Vainio, & Liimatainen, 2018; Paukkonen et al., 2017). Next to structure derived properties like porosity, specific surface and permeability, biocompatibility is a key feature required for these applications. As biocompatibility is inherent to cellulose and its derivatives obtained by oxidative modification (Hujaya et al., 2018; Kumar & Yang, 2002; Mou, Li, Wang, Cha, & Jiang, 2017; Syamala Devi, Sinha, & Vasudevan, 1986), nanocellulose has been gaining considerable attention as building block of novel functional materials for biomedical applications. In particular cellulose nanofibers (CNF) which are highly anisometric nanoparticles consisting of biosynthetically (Fernandes et al., 2011; Sethaphong et al., 2013) aligned cellulose molecules are interesting building blocks in this respect. Next to nanocellulose hydrogels also dried materials such as foams (Löbmann, Wohlert, Müllertz, Wågberg, & Svagan, 2017; Svagan et al., 2016) and aerogels (Li et al., 2019; Zhao et al., 2015) have been proposed for drug delivery. The latter however, require rewetting to trigger the drug release which, in turn, necessitate sufficient dimensional stability to resist capillary forces, but bear the advantage of an easier storage.

CNF can be obtained from virtually any natural cellulose source by mechanical delamination. The required energy input for such processes can be significantly reduced by introduction of repulsive electrostatic forces which can be accomplished by (*e.g.* oxidative) chemical surface modifications. To this end sequential periodate-chlorite oxidation (H. Liimatainen, Visanko, Sirvio, Hormi, & Niinimaki, 2012; Tejado, Alam, Antal, Yang, & van de Ven, 2012) has recently emerged as efficient means of introducing surface charges onto cellulose pulp in form of carboxylate moieties. While (*meta*)periodate selectively and simultaneously converts the two vicinal secondary hydroxyl groups of the anhydroglucose units (AGU) constituting cellulose into aldehydes, chlorite ions further oxidize the latter to carboxyl moieties. The utilized periodate can be easily regenerated by an facile ozone (Koprivica et al., 2016) or hypochlorite treatment (Henrikki Liimatainen, Sirviö, Pajari, Hormi, & Niinimäki, 2013). Mechanical delamination – aided by electrostatic forces of the oxidized pulp cellulose – can yield fully individualized nanofibers, the latter featuring a very low polydispersity with regard to diameter. These CNF are well dispersible in aqueous media and the obtained dispersions are highly stabilized by electrostatic forces arising from the abundant surface charges. Compared to the frequently applied (2,2,6,6-tetramethylpiperidin-1-yl)oxyl-mediated (TEMPO) oxidation (A. Isogai, Saito, & Fukuzumi, 2011) which also promotes mechanical delamination of cellulose, sequential periodate-chlorite oxidation introduces two carboxyl moieties per oxidized AGU (C2,

C3 position) instead of one in C6 position, enabling the introduction of higher surface charge densities.

Self-assembly of individualized cellulose nanofibers into gel and membrane structures can engender highly interfacial anisotropic materials featuring unique properties. Respective CNF membranes have been thus recently tested as templates for transparent, flexible devices (Matti S. Toivonen, Kaskela, Rojas, Kauppinen, & Ikkala, 2015), light diffuser coatings (M. S. Toivonen et al., 2018) and filter devices for aqueous ultra- (M. Visanko et al., 2014; Miikka Visanko, Liimatainen, Sirviö, & Hormi, 2015) and gaseous aerosol- (Nemoto, Saito, & Isogai, 2015; Matti S. Toivonen et al., 2015) filtration. In case the cellulose nanofiber gel-membranes – obtained by slow vacuum filtration assembly – are oven dried to afford dense layers they are referred to as nanopapers (Benítez & Walther, 2017).

In this study we investigate the assembly of nanofibrillated 2,3-dicarboxyl cellulose (*nf*-DCC) or simply "CNF" into anisotropic layered membranes for transdermal drug delivery systems utilizing their high internal surface and tunable content of surface charges for drug loading. In particular loading and release of the potent nonsteroidal anti-inflammatory drug (NSAID) piroxicam (PRX) was investigated. PRX has both analgesic and antipyretic activity and is frequently applied for treatment of acute and chronic rheumatoid arthritis or osteoarthritis (Rafiee-Tehrani & Mehramizi, 2000). However as gastrointestinal disorders (Laporte, Ibanez, Vidal, Vendrell, & Leone, 2004) may occur upon oral administration, transdermal administration (Rafiee-Tehrani & Mehramizi, 2000) is commonly recommended. PRX exhibits poor solubility in many solvents including water potentially constituting an obstacle for its applications. Adsorptive loading of considerable quantities of the drug onto CNF membranes of high PRX affinity and large specific surface is demonstrated to render respective materials attractive as a transdermal drug delivery patch since it overcomes the above obstacle.

## 2 MATERIALS AND METHODS

### 2.1 Materials

Dissolving-grade hardwood pulp (TCF bleached, CCOA (Potthast et al., 2003) 24.3 µmol $g^{-1}$ C=O, FDAM (Bohrn et al., 2006) 13.9 µmol $g^{-1}$ COOH, Mw 303.7 kg $mol^{-1}$, 50 %w) obtained from an industrial magnesium bisulfite process was utilized as starting material. Sodium (meta)periodate, acetic acid, sodium chlorite and sodium hydroxide were purchased (Sigma-Aldrich, Vienna, Austria) at the highest purity grade available and used without further purification. Also, piroxicam (PRX) with a purity of ≥98 % (TLC) was purchased from Sigma-Aldrich and used without further purification. 0.1 M sodium acetate buffer was

prepared by adding 0.1 M acetic acid to a 0.1 M sodium acetate solution until a pH of 5 was reached. Hydrophilic polyvinylidene difluoride (PVDF) membranes (Durapore®, DVPP, Ø 47 mm, H 125 µm, 650 nm pore size) were purchased from Merck KGaA.

### 2.2 Sequential regioselective oxidations

Various oxidative pretreatments based on sequential periodate and chlorite oxidations were investigated as means of pulp modification prior to mechanical delamination of pulp fiber cellulose. The regioselective sequential oxidation (H. Liimatainen et al., 2012; Tejado et al., 2012) is a facile tool for introducing charged moieties (specifically carboxylates) into the pulp materials facilitating delamination and liberation of cellulose nanofibrils.

In brief never-dried dissolving-grade pulp was disintegrated in deionized water using a blender and $NaIO_4$ was added to the pulp suspension to start the first oxidative modification. 1.2 L of 1 wt% pulp suspension was oxidized under constant stirring (600 rpm) using 46 mmol of $NaIO_4$ at 50° C. While the reagent concentration was the same for all variants, reaction time was varied between 2, 3.75 and 4.5 hours to obtain three different degrees of oxidative modification. The reactions were stopped by filtration and washing with deionized water.

The obtained 2,3-dialdehyde cellulose (DAC) samples with different degrees of oxidation were immediately oxidized in a second step by $NaClO_2$ to yield 2,3-dicarboxyl cellulose. For the second oxidative step the entire obtained amount of DAC was suspended in 1 M acetic acid and 12 g of $NaClO_2$ was added and left to react for 40 h under constant agitation. The reaction was stopped again by filtration and extensive washing with deionized water until the electric conductivity dropped below 25 µS $cm^{-1}$. Finally, the concentration of the suspensions was adjusted to 5 g $L^{-1}$ and pH was set to 8 by addition of 0.1 M NaOH to ensure a sufficient amount of $Na^+$ counter ions to saturate the introduced carboxylate moieties.

### 2.3 Mechanical delamination

Suspensions of the oxidatively modified pulp were subjected to repeated high-pressure homogenization until dispersions of individualized cellulose nanoparticles were obtained. In brief, the pulp suspensions (5 g $L^{-1}$, pH 8) were passed two consecutive times through the homogenizer (APV 1000, SPX Flow Technology, USA) at 60 MPa. To ensure complete separation of nanofibers the dispersions were then diluted to 2.5 g $L^{-1}$ and homogenized again by two passes at 80 MPa. Finally, the obtained dispersions were filtered through a POR 3 glass frit to remove any macroscopic residues. Rotoevaporation was employed to concentrate the dispersion to the desired concentration of 5 g $L^{-1}$.

### 2.4 Atomic force microscopy (AFM)

Obtained dispersions were diluted to 5 mg $L^{-1}$ and a drop was dried onto mica discs at 105 °C. AFM scans were taken in tapping mode on a Dimension Icon Scanning Probe Microscope (Bruker AXS, France; formerly Veeco) equipped with OTESPA cantilever and Nano-

Scope V control station. Average dimensions (diameter, length) of CNF were calculated from the size of 30 randomly selected particles per sample.

### 2.5 Determination of carboxyl content

Automated conductometric titration (800 Dosino dosing device connected to an 856 conductivity module both from Metrohm, Switzerland) of the nanofibers was applied to determine the amount of carboxyl moieties on the nanofibers. Nanofiber dispersions (~ 2.5 g $L^{-1}$) were freeze dried at -80° C and 100 mg of dry nanofibers were redispersed in 50 mL deionized water. The dispersions were acidified prior to titration by addition of 2.75 mL of 0.1 M hydrochloric acid. After acid-induced protonation, conductometric titration was accomplished by addition of 25 µL increments of 0.1 M NaOH every 30 seconds. After a total volume of 6 mL had been added, back-titration was conducted by step-wise addition of the same amount of 0.1M HCl (25 µL every 30 seconds). The obtained conductometric titration curves were evaluated by linear fitting and the carboxyl content was calculated as average from both the NaOH and HCl titration curves.

### 2.6 Electrophoretic mobility measurements

The electrophoretic mobility of nanofibers was determined at 25° C by an electrophoretic light scattering instrument (Zetasizer ZS, Malvern Instruments Ltd., U.K.). Dilute nanofiber dispersions were dialyzed against deionized water over two weeks with regular exchange of water to remove excess of sodium ions and other low molecular products potentially present in the dispersions after mechanical delamination. Dialyzed nanofiber dispersions diluted to 500 mg $L^{-1}$ with various NaCl salt concentrations in the range of 2.5 to 100 mM were prepared and measured. The pH was determined with an InLab® Expert Pro pH electrode connected to a seveneasy pH meter (both Mettler Toledo, USA) and adjusted to 6.25 by addition of small quantities of 0.1 M NaOH. All measurements were conducted within hours after the samples had been prepared. The zeta potential was calculated from the electrophoretic mobility according to the Smoluchowski and Ohshima-Henry (Ohshima, 1998; Sato, Kusaka, & Kobayashi, 2017) equations.

### 2.7 Dynamic Light Scattering (DLS)

The size of nanofibers was also evaluated by DLS using a Zetasizer ZS (Malvern Instruments Ltd., Worcestershire, U.K.). Since an accurate measurement of nanofiber length by DLS is difficult, only a comparative estimation was conducted. Dialyzed nanofiber dispersion (500 mg $L^{-1}$) set to pH 6.25 and 25 mM NaCl were measured as triplets with ten acquisitions each. Additionally, DLS was used to monitor potential aggregation of nanofibers in dispersion state.

### 2.8 Membrane preparation

Membranes were formed by vacuum-assisted sedimentation of concentrated aqueous nanofiber dispersions (5 g $L^{-1}$, not dialyzed) using vacuum filtration equipment and hydrophilic PVDF 650 nm filter discs supported on a Pore 3 glass frit. A TRIVAC-E2 two stage oil sealed rotary vane pump was employed to generate reduced pressure of about 10 mbar. After one hour of filtration, excess nanofiber dispersion was poured off and the formed nanofiber membranes together with the PVDF filter were submerged in ethanol for another hour to allow homogeneous mixing with entrapped water. Then the formed nanofiber membrane was carefully peeled off from the PVDF filter support. Sodium counter ions were replaced by $H^+$ ions by placing the membranes for 1 hour into a mixture of 25 %v aqueous 1M HCl and 75 %v ethanol. Thereafter four solvent exchanges steps were conducted aiming to replace the remaining acidic water quantitatively by ethanol using a total ethanol volume equaling 100 times the volume of the membranes.

### 2.9 Field emission electron microscopy of membranes (FEG-SEM)

The morphology of the layered nanofiber membranes was studied by FEG-SEM. Dry membrane samples were prepared by extracting the obtained alcogels submerged in ethanol with supercritical $CO_2$ aiming to avoid any capillary forces that may arise during drying and to preserve the porous membrane structure to full extent. Extraction was performed at 40° C and 9.5 MPa, maintaining a flow rate of 40 g $min^{-1}$ $CO_2$ for 4 hours. The dry samples were gold sputtered with an Edwards S150B and imaged on a Zeiss Supra 55VP (Oberkochen, Germany) using a 0.5-2 kV beam.

### 2.10 Nitrogen sorption of membranes

Pore size distribution and specific surface area (SSA) of the membranes were assessed by nitrogen sorption experiments at 77K using supercritically dried (*cf.* above) samples. Prior to nitrogen sorption all samples were degassed at 50 °C for 20 hours (VacPrep 061, Micromeritics). Nitrogen adsorption and desorption isotherms of the degassed samples were recorded at 77 K on a TriStar II *PLUS* (Micromeritics, Merignac, France). The BET specific surface area was calculated from data points in the range of $p/p^0$ = 0.05-0.2 (ISO, 2010) of the adsorption branch using the Brunauer–Emmett–Teller (BET) equation (Brunauer, Emmett, & Teller, 1938). The pore size distributions of the studied membranes were derived using the Barrett–Joyner–Halenda (BJH) method(Barrett, Joyner, & Halenda, 1951) and applying the Broekhoff–de Boer model (Broekhoff, 1968) on the desorption branch.

### 2.11 Piroxicam loading and release from membranes

Aqueous loading and release of the nonsteroidal anti-inflammatory drug PRX from the various membranes was investigated by UV-Vis spectroscopy using a UV-2600 instrument (Shimadzu, Noisiel, France) quantifying the decrease / increase of PRX in respective aqueous media (see below). Linear PRX calibration curves in deionized water and 0.1 M acetate

buffer (pH 5) were recorded covering the concentration range of 0.2 to 2.5 mg $L^{-1}$ and using the respective absorption maxima at 353 nm and 360 nm.

Prior to drug loading the membranes were placed for 24 hours in excess of deionized water corresponding to 100 times the volume of that of the membranes. The latter were then transferred to a loading bath (400 mL, 25° C) containing 20 mg $L^{-1}$ PRX. Drug loading was monitored throughout the entire residence time of 24 hours by quantifying the decrease of PRX content in the loading bath as effectuated by drug uptake and adsorption onto the nanofiber membranes.

The release of PRX from the nanofiber membranes was accomplished by placing the membranes into 400 mL sodium acetate buffer (0.1 M, pH 5) and quantifying the increase of PRX content in the aqueous phase.

## 3 RESULTS AND DISCUSSION

Sequential oxidative modification and mechanical delamination of the used dissolving pulp afforded entirely individualized cellulose nanofibers (*cf.* Figure 1) which can be referred to as nanofibrillated 2,3-dicarboxyl cellulose (*nf*-DCC) or simply “CNF” to emphasize their similarity to (charged) cellulose nanofibrils obtained by other approaches. Aiming to investigate membrane formation and PRX loading / release for samples of different charge density and nanomorphology, periodate was conducted for different time periods, i.e. 2, 3.75 and 4.5 hours (samples *nf*-DCC 1, *nf*-DCC 2 and *nf*-DCC 3). Conductometric titration confirmed that the duration of periodate oxidation is positively correlated with the amount of introduced carboxyl groups. Correspondingly, the degree of oxidation related to modified anhydroglucose units (AGU) increased in the order *nf*-DCC 1 (6.4%) < *nf*-DCC 2 (14.1%) < *nf*-DCC 3 (16.2%).

The introduced surface charges not only stabilize the nanofiber dispersion, by means of electrostatic repulsion (Fall, Lindstrom, Sundman, Odberg, & Wagberg, 2011), but also facilitate mechanical delamination of the oxidized pulp. This reduces the energy input required to separate and individualize the cellulose nanofibrils considerably (Akira Isogai & Bergström, 2018; A. Isogai et al., 2011; Tejado et al., 2012).

**Table 1: Chemical properties and morphological characteristics of the prepared *nf*-DCC samples.**

| *nf*-DCC | COOH [mmol/g] | DO [%AGU] | Length AFM [nm] | Diameter AFM [nm] | Aspect ratio [-] | Size DLS [nm] |
|---|---|---|---|---|---|---|
| 1 | 0.78±0.03 | 6.36±0.30 | 375.1±203.7 | 2.47±0.67 | 152 | 365.2±68.6 |
| 2 | 1.74±0.03 | 14.10±0.48 | 127.3±46.4 | 2.68±0.69 | 48 | 206.9±52.3 |
| 3 | 2.00±0.11 | 16.16±0.89 | 95.8±53.9 | 2.72±0.95 | 35 | 182.2±10.1 |

Both length and aspect ratio (a) of the nanofibers decreased with the degree of oxidation while the nanofiber diameter remained largely constant (*cf.* Figure 2). The particle size obtained by dynamic light scattering experiments, confirm the decreases of nanofiber length with increasing degree of oxidation (*cf.* Table 1). Yet the difference is less pronounced as suggested by AFM data.

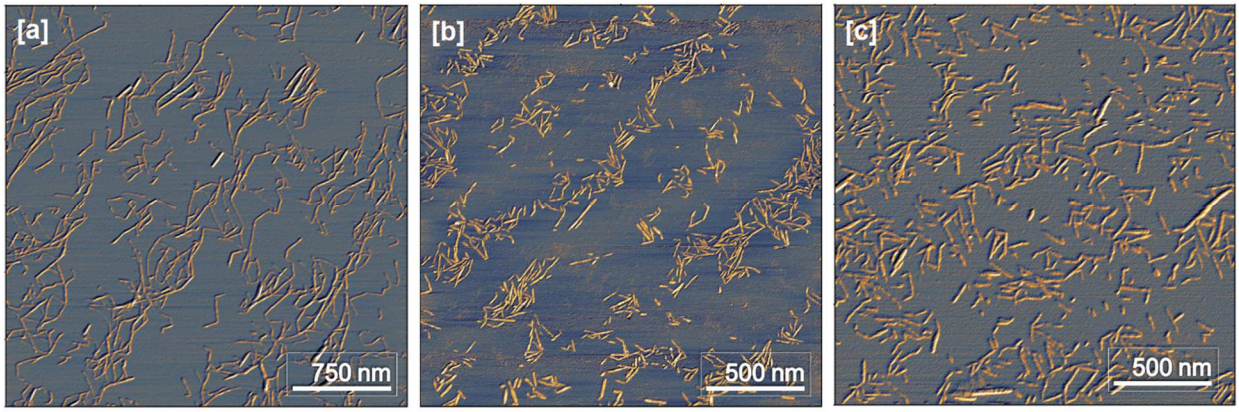


**Figure 1: AFM images of *nf*-DCC samples differing by carboxyl group content (0.78 mmol $g^{-1}$ COOH [a], 1.74 mmol $g^{-1}$ COOH [b], 2.00 mmol $g^{-1}$ COOH [c]).**

Increasing contents of surface carboxyl(ate) moieties were shown to enhance also the electrophoretic mobility, since the nanofiber diameter and hence surface to volume ratio remains largely constant. Zeta potential ($\zeta$) is the electrical potential occurring at the phase boundaries of moving nanoparticles in dispersion state capable of exerting a force on other charged particles. It is commonly calculated from the electrophoretic mobility ($\mu$) is the Smoluchowski equation:

$$\zeta^S = \frac{\eta\mu}{\varepsilon_0\varepsilon_r}$$

Here $\eta$ denotes the viscosity while $\varepsilon_r$ and $\varepsilon_0$ correlate to the relative permittivity and permittivity of free space respectively. Although the Smoluchowski equation is also frequently applied for nanocellulose characterization (Foster et al., 2018; Safari, Sheikhi, & van de Ven, 2014), it can underestimate the zeta potential of cellulose nanofibers at lower salt concentrations (Sato et al., 2017). The small diameters of individualized and well-dispersed cellulose nano-

fibers including the presented *nf*-DCC is in the range of their surrounding electric double layer at lower salt concentration which requires to account for the curvature of the nanofiber. While the Smoluchowski equation is applicable for nanofibers oriented parallel to the electric field, nanofibers in perpendicular orientation is only accurate under consideration of their surface curvature. The electrophoretic mobility of cylinders oriented randomly within an electric field, as we assume for our dilute dispersions, is (De Keizer, Van Der Drift, & Overbeek, 1975):

$$\mu = \frac{\mu_{\parallel} + 2\mu_{\perp}}{3}$$

With $\mu_{\parallel}$ and $\mu_{\perp}$ representing the electrophoretic mobility parallel and orthogonal to the applied electric field respectively. Under consideration of the curvature of cylindrical particles oriented randomly within the electric field the zeta potential can be derived by the Ohshima-Henry (Ohshima, 1998; Sato et al., 2017) equation:

$$\zeta^{OH} = \frac{3\eta\mu}{\varepsilon_r\varepsilon_0\left[2 + \left(1 + \frac{2.55}{\kappa a[1+\exp(-\kappa a)]}\right)^{-2}\right]}$$

When keeping the pH constant (at pH 6.25) the zeta potential decreases with increasing electrolyte concentration (*cf.* Figure 2 d, e and f). This is in accordance with previous studies on carboxylated CNF (Fall et al., 2011; Sato et al., 2017; Wagberg et al., 2008) and cellulose nanocrystals carrying sulfate ester moieties (Prathapan, Thapa, Garnier, & Tabor, 2016). While $\zeta^{S}$ and $\zeta^{OH}$ are in relative good agreement for higher salt concentrations (>50 mM), $\zeta^{OH}$ is considerably higher for lower electrolyte concentrations (<50 mM). While the higher charged nanofiber samples *nf*-DCC 2 and 3 retain their colloidal stability in the studied range up to a 100 mM NaCl concentration, the less charged sample *nf*-DCC 1 reaches the limit of its stability at this salt concentration.

Considering their aspect ratio, the highly charged shorter nanofibers (*nf*-DCC 2 and 3) could also be classified as cellulose nanocrystals obtained by an oxidative mechanical approach rather than conventional acid hydrolysis. (Zhou, Saito, Bergstrom, & Isogai, 2018) However the high amount of surface charges clearly differentiates them from cellulose nanocrystals (Habibi, Lucia, & Rojas, 2010) obtained by acid hydrolysis with zeta potentials of about -30 mV. The amount of surface carboxyl groups on the highly oxidized nanofibrils of the *nf*-DCC 3 sample also exceeds that of previously reported *nf*-DCC (Hujaya et al., 2018; H. Liimatainen et al., 2012; Plappert, Nedelec, Rennhofer, Lichtenegger, & Liebner, 2017; M. Visanko et al., 2014).

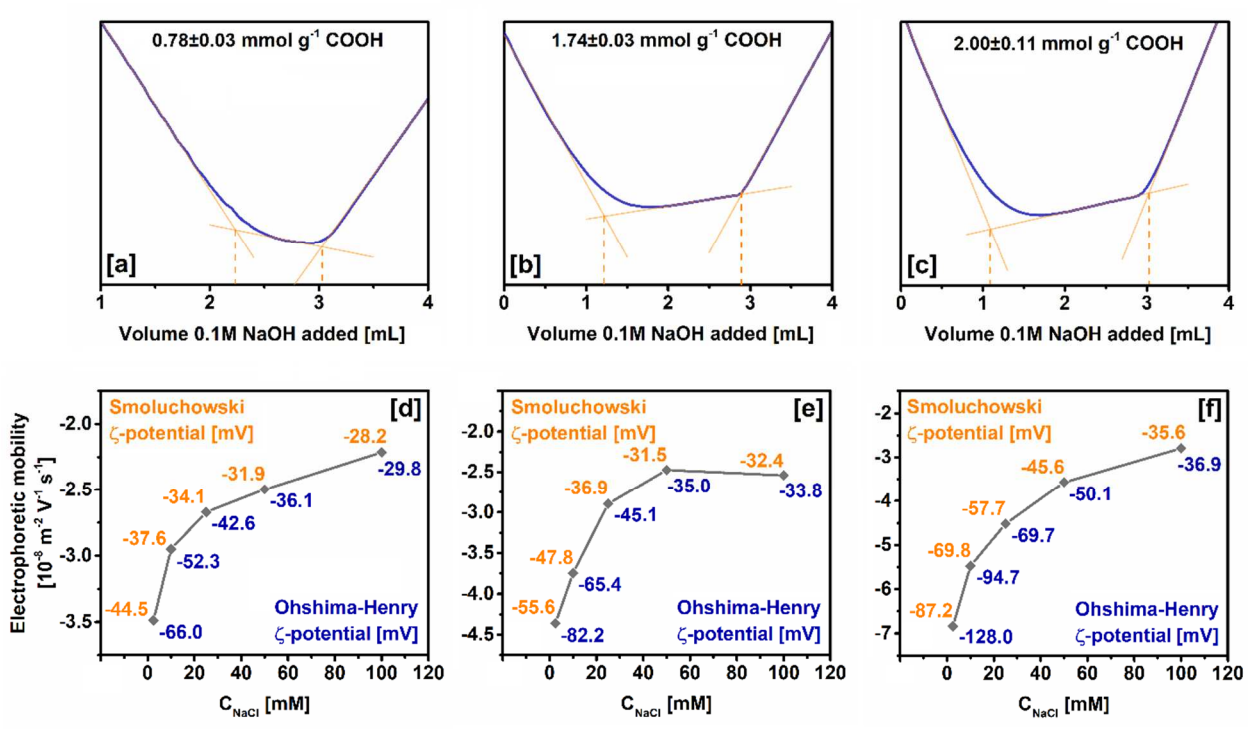


**Figure 2: Conductive titration curves (a, b and c) of *nf*-DCC (100 mg, protonated form) dispersions and electrophoretic mobility (d, e and f) of corresponding dialyzed *nf*-DCC samples at different salt (NaCl) concentrations. Zeta potentials were calculated using the Smoluchowski and Ohshima–Henry equations (Ohshima, 1998; Sato et al., 2017), respectively.**

Compared to TEMPO-mediated oxidation (A. Isogai et al., 2011) which is frequently applied for the preparation of CNF, sequential periodate-chlorite oxidation can be regarded superior for the introduction of higher amounts of surface charges. TEMPO oxidation relying on the electron transfer capabilities of a stable nitroxyl radical selectively converts the primary hydroxyl groups in C6 position of the AGU into carboxyl(ate) moieties (A. Isogai et al., 2011). Provided quantitative turnover, TEMPO-mediated oxidation maximally yields one carboxyl moiety per oxidized AGU. Sequential periodate-chlorite oxidation on the other hand simultaneously introduces two carboxyl moieties per oxidized AGU. On crystalline cellulose I surfaces TEMPO-mediated oxidation can only oxidize every second AGU due to the 180° rotation of every second AGU within the cellulose chain (Montanari, Roumani, Heux, & Vignon, 2005; Shinoda, Saito, Okita, & Isogai, 2012). For these limitations, zeta potential does not exceed -75 mV, hence limiting colloidal stability for CNF obtained by TEMPO oxidation regardless of the type of cellulose I substrate used (Okita, Saito, & Isogai, 2010).

Highly anisometric colloids such as the well-dispersed CNF of this study can exhibit decreased degrees of (translational and rotational) freedom in dispersions of low solid content and volume fraction, respectively (Mendoza, Batchelor, Tabor, & Garnier, 2018; Nordenstrom, Fall, Nystrom, & Wagberg, 2017; Solomon & Spicer, 2010). The solid content of the 0.5 wt% dispersions utilized for membrane formation corresponds to a 0.3 % volume fraction ($\varphi$). At this semi-dilute state ($a^{-2} < \varphi < a^{-1}$) the nanofiber's translational freedom is already restricted

whereas rotation around and vibration along the axis is not affected. Therefore, respective dispersions flow easily even though the nanofibers are entangled to some extent. Filtration of semi-dilute nanofiber dispersions therefore yields entangled layered gel structures. Submerging the formed anisotropic gels in the cellulose non-solvent ethanol leads to a strengthening of the structure due to the removal of tightly bound surface water as well-known from cellulose hornification. Moreover protonation of carboxyl moieties on the nanofiber surface as accomplished by acidification diminishes electrostatic repulsion (Fall et al., 2011; Mendoza et al., 2018) and enables further inter-particulate hydrogen bonding and van der waals interactions. Exchange of sodium ions by protons ($H^+$ ions) is also paramount for electrostatic adsorption of charged drug molecules.

The final membranes had a thickness of about 1 mm and a largely consistent *nf*-DCC content of about 22 mg $cm^{-3}$ corresponding to a volume fraction of about 1.4 % compared while the employed CNF dispersion had a volume fraction of 0.3 %.

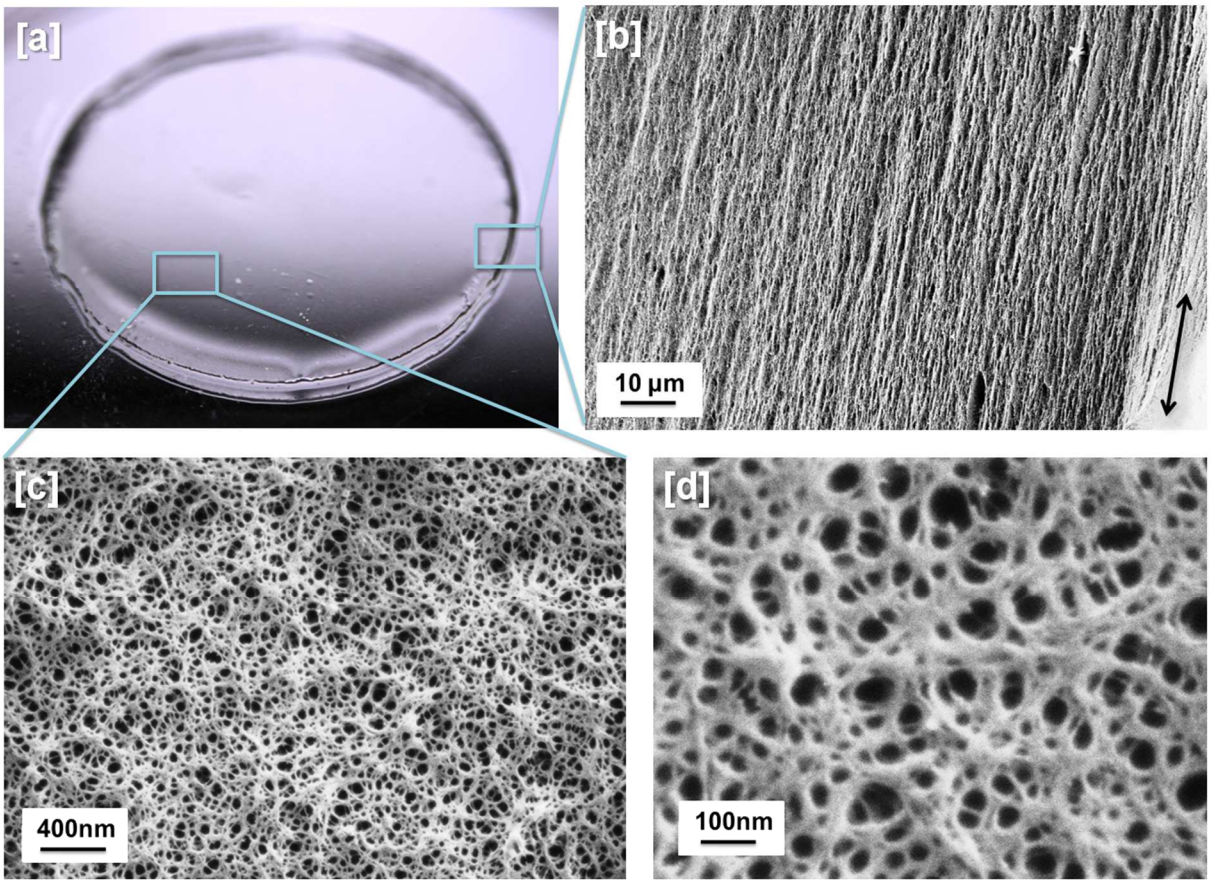


**Figure 3: Picture of the *nf*-DCC 2 membrane [a] and corresponding FEG-SEM images showing the horizontally layered structure [b] and the nanoporous surface [c] and [d] at different magnifications.**

Supercritical fluid extraction allows for drying the *nf*-DCC gel (Plappert et al., 2017) membrane without causing structural damage to the nanofiber structure which would arise from capillary forces during conventional drying. This allowed for a detailed characterization of the anisotropic membranes by field emission gun scanning electron microscope (FEG-SEM) and

gas sorption experiments which would have been not feasible in wet state. The obtained FEG-SEM micrographs clearly show the layered nanofiber architecture of the membranes (*cf.* Figure 3b) and reveal their interconnected nanoporosity constituted of voids not larger than 100 nm (*cf.* Figure 3 c, d).

**Table 2: Bulk density of $scCO_2$ dried *nf*-DCC membranes and internal surface characteristics as determined by nitrogen sorption experiments at 77K.**

| *nf*-DCC | Membrane density [mg $cm^{-3}$] | Specific surface area [$m^2$ $g^{-1}$] | C-value (BET) [-] |
|---|---|---|---|
| 1 | 21 | 502 | 107 |
| 2 | 22 | 452 | 87 |
| 3 | 22 | 349 | 68 |

Nitrogen sorption isotherms of $scCO_2$-dried *nf*-DCC membranes as recorded at 77 K correspond in shape the IUPAC type IV characteristic for mesoporous materials (Thommes et al., 2015). The pore size distribution calculated according to the BJH method was for all membranes centered around a maximum at about 40 nm. However, membranes composed of the longer *nf*-DCC 1 fibrils feature a considerably larger amount of mesopores compared to the other two membranes which are composed of shorter nanofibers (*nf*-DCC 2 and 3). On the other hand, the latter had also a considerable amount of small mesopores (< 10 nm). As suggested by BET calculations, all samples featured high specific surface areas ranging from 350 to 450 $m^2$ $g^{-1}$ for the membranes composed of shorter nanofibers (*nf*-DCC 2 and 3) up to 500 $m^2$ $g^{-1}$ for the membranes composed of the longer nanofibers (*nf*-DCC 1). The specific surface of the prepared membranes is in good agreement with that of previously reported aerogels (Plappert et al., 2017) which were obtained by acid- induced gelation of nematically structured *nf*-DCC dispersions followed by $scCO_2$ drying. The BET constant $C_{BET}$(Sing, 2001) indicating the affinity of $N_2$ for the surface decreased with increasing amount of surface carboxyl moieties. This could be an indication for adsorbed water (Orsolini et al., 2015) which remains on the membrane surface as hydrophilicity increases with the amount of introduced carboxyl moieties and could interfere with nitrogen adsorption.

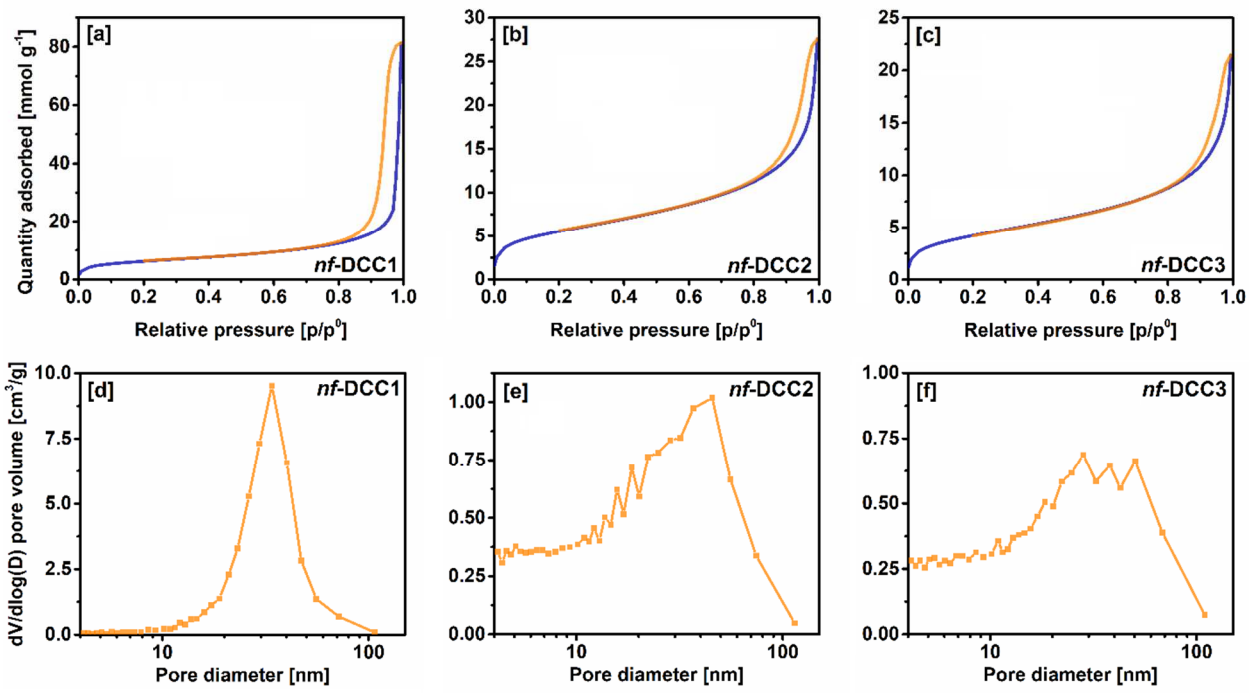


**Figure 4: Nitrogen adsorption (blue) and desorption (orange) isotherms [a, b and c]. Pore size distribution obtained via the BJH methods on the desorption branches of the isotherms [d, e and f] for respective *nf*-DCC membrane samples.**

Upon placing the membranes in water prior to drug loading the membranes soften, become more elastic and swell again. When the membrane is immersed in the loading bath containing piroxicam (PRX), the zwitterionic drug infuses the highly porous nanofiber scaffold and adsorbs onto its large internal surface. Depending on the solvent environment PRX can form various tautomers including a zwitterionic structure in aqueous environments (Gil & Douhal, 2008; Ivanova et al., 2015). Due to the comparatively low p$K_a$ value of its pyridyl nitrogen moiety, a cationic PRX tautomer is prevalent in acidic aqueous environments (Gil & Douhal, 2008). This has been spectroscopically verified by the slight red shift (353 → 360 nm) of its adsorption maximum (Gil & Douhal, 2008) and was confirmed for a PRX solution in 0.1 M acetic acid buffer at pH 5 (*cf.* supporting information S2).

The high specific surface of CNF based materials has great potential with regard to adsorption of poorly water-soluble drugs (Lobmann & Svagan, 2017). This has been previously demonstrated for the sulfonamide derivative furosemide, a drug that is frequently used for treatment of hypertension and edema. It has been shown that adsorption is here governed by specific surface rather than by surface charge which has been explained by the specific mode of adsorption relating to deposition of the planar aryl moieties onto hydrophobic domains of cellulose and the resulting gain in entropy driven by release of surface bound water (Lombardo et al., 2018). Different from furosemide, a positive correlation between surface charge density and amount of adsorbed drug was found for piroxicam (*cf.* Figure 5) when loaded in zwitterionic form at near neutral pH. This suggests electrostatic adsorption of the drug molecule at the *nf*-DCC interfaces which still requires a high specific surface area in

addition to an adequate surface charge density. Considering a zwitterionic structure prevailing for PRX at loading conditions and the pKa range of the carboxyl groups residing at the interface of the *nf*-DCC membranes (p$K_a$ 3.66-4.76) (Kim & Kuga, 2001), it is safe to assume that PRX will adsorb as cation and establish an electric double layer around the *nf*-DCC surface. PRX loading curves (Figure 5a-c) reveal that the equilibrium adsorption state had been reached for all membrane samples after 24 hours of residence time in the loading bath. The adsorbed amounts of PRX ranged from 30 to 60 mg per g of *nf*-DCC, depending on surface charge of the respective *nf*-DCC interfaces. Considering the *nf*-DCC density of the prepared membranes (22 mg $cm^{-3}$), a maximum loading of 1.32 mg $cm^{-3}$ could be achieved which exceeds the loading bath concentration (0.02 mg $cm^{-3}$) by a factor of 66.

The release of PRX from the *nf*-DCC membranes was investigated using 0.1 M acetate buffer (pH 5) as these conditions resemble the slightly acidic nature and electrolyte content of human skin (Draize, 1942). Release of the drug is triggered by the electrolyte infusing the membranes and gradually weakening electrostatic forces between the cationic drug molecules and the anionic membrane surfaces mainly by electrostatic shielding and cation exchange.

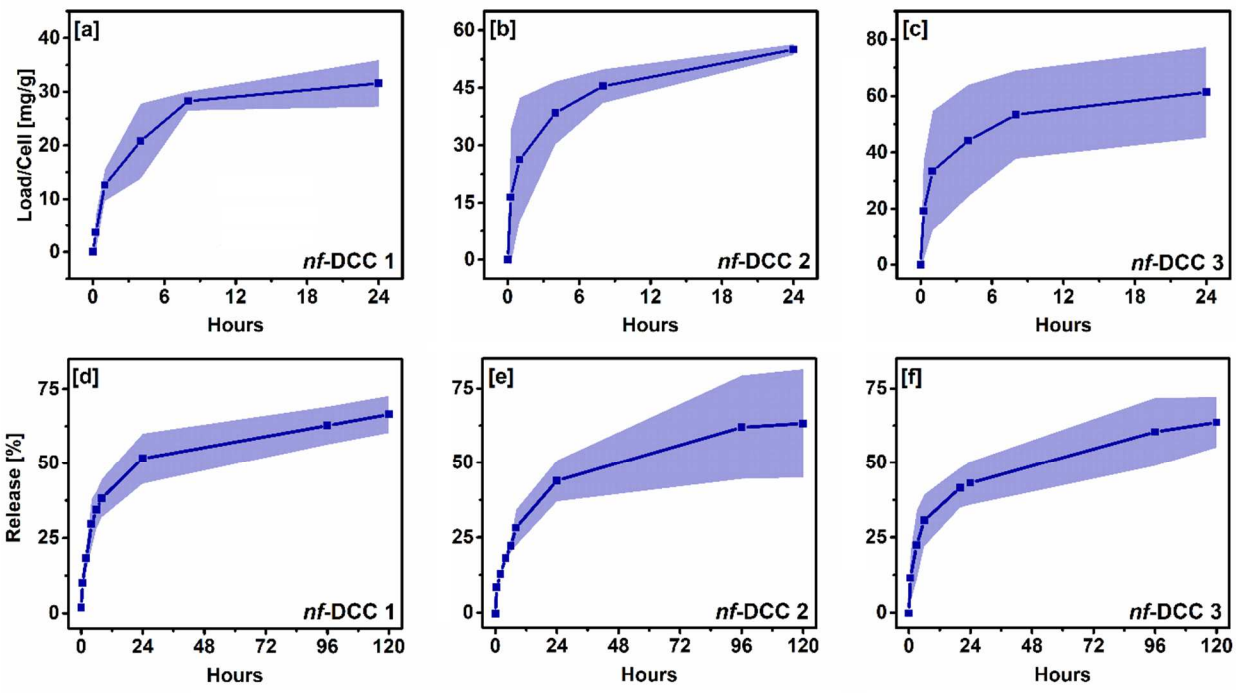


**Figure 5: Piroxicam loading in zwitter-ionic form (a-c, pH ≈ 6.8) and release as cation (c-e, acetate buffer pH 5) for membranes composed of *nf*-DCC 1 (a, d), 2 (b, e) and 3 (c, f) with the standard deviations displayed as shaded areas.**

The PRX release could be triggered by the induced pH change as well, however, this was not further investigated since it was not considered relevant for transdermal drug delivery but could be meaningful for oral drug administration.

All tested membranes released piroxicam at somewhat slower rate compared to its loading from near-neutral aqueous phase. Both uptake and release are characterized by high initial

adsorption and desorption rates that increasingly abate with time. Compared to previously reported CNF nanopapers (Löbmann et al., 2017) the release is the drug molecules is significantly increased. During preparation of such Nanopapers or films the porous structure and surface of the CNF is typically lost. On the other hand, the here described wet drug loading and release of CNF membranes utilizes the anisotropic porous gel structure feature high specific surface areas (*cf.* BET) for drug molecule adsorption and release. This enables to exploit the full potential of CNF as high surface area nanoparticles and demonstrates their applicability for aqueous sorption processes. Therefore the comparatively long equilibration times for both the loading and unloading process can be attributed at least in part to the high surface area mesoporous structure of the membranes which impedes diffusion of the drug molecules due to long, windy and tortuous narrow pathways through the *nf*-DCC scaffolds. Due to the layered alignment of the nanofibers, diffusion orthogonal to the membrane plane – which corresponds to the mode of drug delivery for an application as transdermal patches – is stronger retarded than in plane. Compared to the aerogels materials (Ulker & Erkey, 2014; Zhao et al., 2015) the need for a employing supercritical drying of freeze drying technology is completely avoided by utilizing the gel membranes in the wet state while similar release times and profiles were observed.

## 4 CONCLUSION

Sequential periodate-chlorite oxidation of pulp cellulose prior to mechanical delamination – employed to obtain well isolated cellulose nanofibrils – has been demonstrated to be an efficient measure to tune the surface charge of the nanoparticles in terms of carboxylate group content within the range of 0.74 to 2.00 mmol $g^{-1}$. While the completely individualized nanofibers all share similar diameters of about 2.5 nm, both length and aspect ratio decreased with increasing degree of oxidation. For the longest oxidation periods tested, the average length of the nanofibers dropped from about 375 to 95 nm (AFM) compared to short-term oxidation. This trend was confirmed by DLS.

The variation in DO allows for tuning the range of surface charge density as evident from electrophoretic mobility of respective dispersions that was determined for various electrolyte concentrations (2.5 to 100 mM NaCl). The Zeta potential of 0.05% (w/v) *nf*-DCC dispersions in aqueous 2.5 mM sodium chloride as calculated using the Smoluchowski equation varied from -44.5 to -87.2 mV and confirms that.increasing electrolyte concentrations entails a respective decrease of zeta potential.

*nf*-DCC nanofibers were assembled into anisotropic layered gel membranes by vacuum filtration. Treatment of the membranes with aqueous hydrochloric acid transforms surface carboxylate ions into carboxyl groups and triggers gel formation by interparticulate hydrogen bonding. Supercritical $CO_2$ extraction of the gel membranes after replacing the interstitial

water by ethanol – a solvent fully miscible with $CO_2$ – allowed the nanomorphological characterization of the scaffold structures without causing any damage by the drying procedure. FEG-SEM images of the anisotropic membranes and nitrogen sorption experiments revealed a relatively narrow pore size distribution peaking at about 40 nm. Specific surface as determined by nitrogen sorption at 77K using the BET approach ranged from 350 to 500 $m^2 g^{-1}$ with membranes composed of longer nanofibers featuring higher SSA values and higher nanopore volumes than membranes made from shorter nanofibers. Loading of wet membranes with the nonsteroidal anti-inflammatory drug piroxicam suggests that adsorption of the drug at near neutral pH is driven by electrostatic attraction between the cationic drug and the anionic internal surface of the *nf*-DCC membranes. This is evident from the extent of drug loading (30-60 mg $g^{-1}$) which increased with surface charge density. Release of the drug into acetate buffer resembling human skin conditions was found to require longer time periods compared to the loading process. This confirms the applicability of the nanofiber membranes as patches for transdermal drug delivery. Furthermore, the anisotropic layered nanoporous structure of the membranes holds great potential for prolonged drug release orthogonal to the plane of the membrane.

## 5 ACKNOWLEDGEMENTS

Financial support by the French Agence Nationale de la Recherche (ANR-15-CE18-0031, OA-ANGIO-ANALGESIA) and the Austrian BMLFUW Ministry (WoodWisdom-Net+ project AeroWood) is gratefully acknowledged.

## 6 REFERENCES

Abeer, M. M., Mohd Amin, M. C., & Martin, C. (2014). A review of bacterial cellulose-based drug delivery systems: their biochemistry, current approaches and future prospects. *J. Pharm. Pharmacol.,* 66(8), 1047-1061.

Ahrem, H., Pretzel, D., Endres, M., Conrad, D., Courseau, J., Muller, H., . . . Kinne, R. W. (2014). Laser-structured bacterial nanocellulose hydrogels support ingrowth and differentiation of chondrocytes and show potential as cartilage implants. *Acta Biomater.,* 10(3), 1341-1353.

Barrett, E. P., Joyner, L. G., & Halenda, P. P. (1951). The Determination of Pore Volume and Area Distributions in Porous Substances. I. Computations from Nitrogen Isotherms. *J. Am. Chem. Soc.,* 73(1), 373-380.

Benítez, A. J., & Walther, A. (2017). Cellulose nanofibril nanopapers and bioinspired nanocomposites: a review to understand the mechanical property space. *J. Mater. Chem. A,* 5(31), 16003-16024.

Bohrn, R., Potthast, A., Schiehser, S., Rosenau, T., Sixta, H., & Kosma, P. (2006). The FDAM method: determination of carboxyl profiles in cellulosic materials by combining group-selective fluorescence labeling with GPC. *Biomacromolecules,* 7(6), 1743-1750.

Bonilla, M. R., Lopez-Sanchez, P., Gidley, M. J., & Stokes, J. R. (2016). Micromechanical model of biphasic biomaterials with internal adhesion: Application to nanocellulose hydrogel composites. *Acta Biomater.,* 29, 149-160.

Broekhoff, J. (1968). Studies on pore systems in catalysts XIII. Pore distributions from the desorption branch of a nitrogen sorption isotherm in the case of cylindrical pores B. Applications. *J. Catal.,* 10(4), 377-390.

Brunauer, S., Emmett, P. H., & Teller, E. (1938). Adsorption of Gases in Multimolecular Layers. *J. Am. Chem. Soc.,* 60(2), 309-319.

De Keizer, A., Van Der Drift, W. P. J. T., & Overbeek, J. T. G. (1975). Electrophoresis of randomly oriented cylindrical particles. *Biophys. Chem.,* 3(1), 107-108.

Deng, H., Zhou, X., Wang, X., Zhang, C., Ding, B., Zhang, Q., & Du, Y. (2010). Layer-by-layer structured polysaccharides film-coated cellulose nanofibrous mats for cell culture. *Carbohydr. Polym.,* 80(2), 474-479.

Draize, J. H. (1942). The Determination of the pH of the Skin of Man and Common Laboratory Animals. *J. Invest. Dermatol.,* 5(2), 77-85.

Fall, A. B., Lindstrom, S. B., Sundman, O., Odberg, L., & Wagberg, L. (2011). Colloidal stability of aqueous nanofibrillated cellulose dispersions. *Langmuir,* 27(18), 11332-11338.

Fernandes, A. N., Thomas, L. H., Altaner, C. M., Callow, P., Forsyth, V. T., Apperley, D. C., . . . Jarvis, M. C. (2011). Nanostructure of cellulose microfibrils in spruce wood. *Proc. Natl. Acad. Sci. U. S. A.,* 108(47), E1195-1203.

Foster, E. J., Moon, R. J., Agarwal, U. P., Bortner, M. J., Bras, J., Camarero-Espinosa, S., . . . Youngblood, J. (2018). Current characterization methods for cellulose nanomaterials. *Chem. Soc. Rev.,* 47(8), 2609-2679.

Gil, M., & Douhal, A. (2008). Femtosecond dynamics of piroxicam structures in solutions. *J. Phys. Chem., A,* 112(36), 8231-8237.

Habibi, Y., Lucia, L. A., & Rojas, O. J. (2010). Cellulose nanocrystals: chemistry, self-assembly, and applications. *Chem. Rev.,* 110(6), 3479-3500.

Hakkarainen, T., Koivuniemi, R., Kosonen, M., Escobedo-Lucea, C., Sanz-Garcia, A., Vuola, J., . . . Kavola, H. (2016). Nanofibrillar cellulose wound dressing in skin graft donor site treatment. *J. Control. Release,* 244(Pt B), 292-301.

Hujaya, S. D., Lorite, G. S., Vainio, S. J., & Liimatainen, H. (2018). Polyion complex hydrogels from chemically modified cellulose nanofibrils: Structure-function relationship and potential for controlled and pH-responsive release of doxorubicin. *Acta Biomater.*

ISO. (2010). Determination of the specific surface area of solids by gas adsorption — BET method. (Vol. ISO 9277).

Isogai, A., & Bergström, L. (2018). Preparation of cellulose nanofibers using green and sustainable chemistry. *Current Opinion in Green and Sustainable Chemistry,* 12, 15-21.

Isogai, A., Saito, T., & Fukuzumi, H. (2011). TEMPO-oxidized cellulose nanofibers. *Nanoscale,* 3(1), 71-85.

Ivanova, D., Deneva, V., Nedeltcheva, D., Kamounah, F. S., Gergov, G., Hansen, P. E., . . . Antonov, L. (2015). Tautomeric transformations of piroxicam in solution: a combined experimental and theoretical study. *RSC Adv.,* 5(40), 31852-31860.

Kim, U.-J., & Kuga, S. (2001). Ion-exchange chromatography by dicarboxyl cellulose gel. *J. Chromatogr. A,* 919, 29-37.

Koprivica, S., Siller, M., Hosoya, T., Roggenstein, W., Rosenau, T., & Potthast, A. (2016). Regeneration of Aqueous Periodate Solutions by Ozone Treatment: A Sustainable Approach for Dialdehyde Cellulose Production. *ChemSusChem,* 9(8), 825-833.

Kumar, V., & Yang, T. (2002). HNO3/H3PO4–NANO2 mediated oxidation of cellulose — preparation and characterization of bioabsorbable oxidized celluloses in high yields and with different levels of oxidation. *Carbohydr. Polym.,* 48(4), 403-412.

Laporte, J.-R., Ibanez, L., Vidal, X., Vendrell, L., & Leone, R. (2004). Upper Gastrointestinal Bleeding Associated with the Use of NSAIDs. *Drug Safety,* 27(6), 411-420.

Leppiniemi, J., Lahtinen, P., Paajanen, A., Mahlberg, R., Metsa-Kortelainen, S., Pinomaa, T., . . . Hytonen, V. P. (2017). 3D-Printable Bioactivated Nanocellulose-Alginate Hydrogels. *ACS Appl. Mater. Interfaces,* 9(26), 21959-21970.

Li, X., Liu, Y., Yu, Y., Chen, W., Liu, Y., & Yu, H. (2019). Nanoformulations of quercetin and cellulose nanofibers as healthcare supplements with sustained antioxidant activity. *Carbohydr. Polym.,* 207, 160-168.

Liimatainen, H., Sirviö, J., Pajari, H., Hormi, O., & Niinimäki, J. (2013). Regeneration and Recycling of Aqueous Periodate Solution in Dialdehyde Cellulose Production. *J. Wood Chem. Technol.,* 33(4), 258-266.

Liimatainen, H., Visanko, M., Sirvio, J. A., Hormi, O. E., & Niinimaki, J. (2012). Enhancement of the nanofibrillation of wood cellulose through sequential periodate-chlorite oxidation. *Biomacromolecules,* 13(5), 1592-1597.

Liu, S., Jin, M., Chen, Y., Gao, H., Shi, X., Cheng, W., . . . Wang, Y. (2017). High internal phase emulsions stabilised by supramolecular cellulose nanocrystals and their application as cell-adhesive macroporous hydrogel monoliths. *J. Mater. Chem. B,* 5(14), 2671-2678.

Lobmann, K., & Svagan, A. J. (2017). Cellulose nanofibers as excipient for the delivery of poorly soluble drugs. *Int. J. Pharm.,* 533(1), 285-297.

Löbmann, K., Wohlert, J., Müllertz, A., Wågberg, L., & Svagan, A. J. (2017). Cellulose Nanopaper and Nanofoam for Patient-Tailored Drug Delivery. *Adv. Mater. Interfaces,* 4(9), 1600655.

Lombardo, S., Chen, P., Larsson, P. A., Thielemans, W., Wohlert, J., & Svagan, A. J. (2018). Toward Improved Understanding of the Interactions between Poorly Soluble Drugs and Cellulose Nanofibers. *Langmuir,* 34(19), 5464-5473.

Mendoza, L., Batchelor, W., Tabor, R. F., & Garnier, G. (2018). Gelation mechanism of cellulose nanofibre gels: A colloids and interfacial perspective. *J. Colloid Interface Sci.,* 509, 39-46.

Montanari, S., Roumani, M., Heux, L., & Vignon, M. R. (2005). Topochemistry of Carboxylated Cellulose Nanocrystals Resulting from TEMPO-Mediated Oxidation. *Macromolecules,* 38(5), 1665-1671.

Mou, K., Li, J., Wang, Y., Cha, R., & Jiang, X. (2017). 2,3-Dialdehyde nanofibrillated cellulose as a potential material for the treatment of MRSA infection. *J. Mater. Chem. B,* 5(38), 7876-7884.

Nemoto, J., Saito, T., & Isogai, A. (2015). Simple Freeze-Drying Procedure for Producing Nanocellulose Aerogel-Containing, High-Performance Air Filters. *ACS Appl. Mater. Interfaces,* 7(35), 19809-19815.

Nordenstrom, M., Fall, A., Nystrom, G., & Wagberg, L. (2017). Formation of Colloidal Nanocellulose Glasses and Gels. *Langmuir,* 33(38), 9772-9780.

Ohshima, H. (1998). Surface Charge Density/Surface Potential Relationship for a Cylindrical Particle in an Electrolyte Solution. *J. Colloid Interface Sci.,* 200(2), 291-297.

Okita, Y., Saito, T., & Isogai, A. (2010). Entire surface oxidation of various cellulose microfibrils by TEMPO-mediated oxidation. *Biomacromolecules,* 11(6), 1696-1700.

Orsolini, P., Michen, B., Huch, A., Tingaut, P., Caseri, W. R., & Zimmermann, T. (2015). Characterization of Pores in Dense Nanopapers and Nanofibrillated Cellulose Membranes: A Critical Assessment of Established Methods. *ACS Appl. Mater. Interfaces.,* 7(46), 25884-25897.

Paukkonen, H., Kunnari, M., Lauren, P., Hakkarainen, T., Auvinen, V. V., Oksanen, T., . . . Laaksonen, T. (2017). Nanofibrillar cellulose hydrogels and reconstructed hydrogels as matrices for controlled drug release. *Int. J. Pharm.,* 532(1), 269-280.

Plappert, S. F., Nedelec, J.-M., Rennhofer, H., Lichtenegger, H. C., & Liebner, F. W. (2017). Strain Hardening and Pore Size Harmonization by Uniaxial Densification: A Facile Approach toward Superinsulating Aerogels from Nematic Nanofibrillated 2,3-Dicarboxyl Cellulose. *Chem. Mater.,* 29(16), 6630-6641.

Potthast, A., Rohrling, J., Rosenau, T., Borgards, A., Sixta, H., & Kosma, P. (2003). A novel method for the determination of carbonyl groups in cellulosics by fluorescence labeling. 3. Monitoring oxidative processes. *Biomacromolecules,* 4(3), 743-749.

Prathapan, R., Thapa, R., Garnier, G., & Tabor, R. F. (2016). Modulating the zeta potential of cellulose nanocrystals using salts and surfactants. *Colloids Surf., A,* 509, 11-18.

Rafiee-Tehrani, M., & Mehramizi, A. (2000). In vitro release studies of piroxicam from oil-in-water creams and hydroalcoholic gel topical formulations. *Drug. Dev. Ind. Pharm.,* 26(4), 409-414.

Safari, S., Sheikhi, A., & van de Ven, T. G. (2014). Electroacoustic characterization of conventional and electrosterically stabilized nanocrystalline celluloses. *J. Colloid Interface Sci.,* 432, 151-157.

Sato, Y., Kusaka, Y., & Kobayashi, M. (2017). Charging and Aggregation Behavior of Cellulose Nanofibers in Aqueous Solution. *Langmuir,* 33(44), 12660-12669.

Sethaphong, L., Haigler, C. H., Kubicki, J. D., Zimmer, J., Bonetta, D., DeBolt, S., & Yingling, Y. G. (2013). Tertiary model of a plant cellulose synthase. *Proc. Natl. Acad. Sci. U. S. A.,* 110(18), 7512-7517.

Shinoda, R., Saito, T., Okita, Y., & Isogai, A. (2012). Relationship between length and degree of polymerization of TEMPO-oxidized cellulose nanofibrils. *Biomacromolecules,* 13(3), 842-849.

Sing, K. (2001). The use of nitrogen adsorption for the characterisation of porous materials. *Colloids Surf., A,* 187-188, 3-9.

Solomon, M. J., & Spicer, P. T. (2010). Microstructural regimes of colloidal rod suspensions, gels, and glasses. *Soft Matter,* 6(7), 1391–1400.

Svagan, A. J., Benjamins, J. W., Al-Ansari, Z., Shalom, D. B., Mullertz, A., Wagberg, L., & Lobmann, K. (2016). Solid cellulose nanofiber based foams - Towards facile design of sustained drug delivery systems. *J. Control. Release,* 244(Pt A), 74-82.

Syamala Devi, K., Sinha, T. J., & Vasudevan, P. (1986). Biosoluble surgical material from 2,3-dialdehyde cellulose. *Biomaterials,* 7(3), 193-196.

Tejado, A., Alam, M. N., Antal, M., Yang, H., & van de Ven, T. G. M. (2012). Energy requirements for the disintegration of cellulose fibers into cellulose nanofibers. *Cellulose,* 19(3), 831-842.

Thommes, M., Kaneko, K., Neimark, A. V., Olivier, J. P., Rodriguez-Reinoso, F., Rouquerol, J., & Sing, K. S. W. (2015). Physisorption of gases, with special reference to the evaluation of surface area and pore size distribution (IUPAC Technical Report). *Pure Appl. Chem.,* 87(9-10).

Toivonen, M. S., Kaskela, A., Rojas, O. J., Kauppinen, E. I., & Ikkala, O. (2015). Ambient-Dried Cellulose Nanofibril Aerogel Membranes with High Tensile Strength and Their Use for Aerosol Collection and Templates for Transparent, Flexible Devices. *Adv. Funct. Mater.,* 25(42), 6618-6626.

Toivonen, M. S., Onelli, O. D., Jacucci, G., Lovikka, V., Rojas, O. J., Ikkala, O., & Vignolini, S. (2018). Anomalous-Diffusion-Assisted Brightness in White Cellulose Nanofibril Membranes. *Adv. Mater.,* 30(16), e1704050.

Ulker, Z., & Erkey, C. (2014). An emerging platform for drug delivery: aerogel based systems. *J Control Release,* 177, 51-63.

Van Vlierberghe, S., Dubruel, P., & Schacht, E. (2011). Biopolymer-based hydrogels as scaffolds for tissue engineering applications: a review. *Biomacromolecules,* 12(5), 1387-1408.

Visanko, M., Liimatainen, H., Sirvio, J. A., Haapala, A., Sliz, R., Niinimaki, J., & Hormi, O. (2014). Porous thin film barrier layers from 2,3-dicarboxylic acid cellulose nanofibrils for membrane structures. *Carbohydr. Polym.,* 102, 584-589.

Visanko, M., Liimatainen, H., Sirviö, J. A., & Hormi, O. (2015). A cross-linked 2,3-dicarboxylic acid cellulose nanofibril network: A nanoporous thin-film layer with tailored pore size for composite membranes. *Sep. Purif. Technol.,* 154, 44-50.

Wagberg, L., Decher, G., Norgren, M., Lindstrom, T., Ankerfors, M., & Axnas, K. (2008). The build-up of polyelectrolyte multilayers of microfibrillated cellulose and cationic polyelectrolytes. *Langmuir,* 24(3), 784-795.

Zaborowska, M., Bodin, A., Backdahl, H., Popp, J., Goldstein, A., & Gatenholm, P. (2010). Microporous bacterial cellulose as a potential scaffold for bone regeneration. *Acta Biomater.,* 6(7), 2540-2547.

Zhao, J., Lu, C., He, X., Zhang, X., Zhang, W., & Zhang, X. (2015). Polyethylenimine-grafted cellulose nanofibril aerogels as versatile vehicles for drug delivery. *ACS Appl. Mater. Interfaces,* 7(4), 2607-2615.

Zhou, Y., Saito, T., Bergstrom, L., & Isogai, A. (2018). Acid-Free Preparation of Cellulose Nanocrystals by TEMPO Oxidation and Subsequent Cavitation. *Biomacromolecules,* 19(2), 633-639.